Supplemental Document [Compiled on December 6, 2024]

Sébastien Crombez[1,2], Cédric Ray[1,2], Chloé Exbrayat-Héritier[3], Florence Ruggiero[3], Nicolas Ducros[1,4*]

[1]INSA-Lyon, Université Claude Bernard Lyon 1, CNRS, Inserm, CREATIS UMR 5220, U1294, F-69621, LYON, France.
[2]Université Claude Bernard Lyon 1, CNRS, Institut Lumière Matière, F-69622, Villeurbanne, France.
[3]Institut de Génomique Fonctionnelle de Lyon, ENS-Lyon, UMR CNRS 5242, Universite Claude Bernard Lyon 1, Lyon Cedex, France.
[4]Institut Universitaire de France, France.

*Corresponding author(s). E-mail(s): nicolas.ducros@creatis.insa-lyon.fr;

1 Experimental setup

Our optical system is shown in Figure 1. It is powered by two continuous lasers, which emit at $\lambda = 473$ nm (MBL-FN-473, CNI®) and $\lambda = 532$ nm (MBL-FN-532, CNI®), combined with a dichroic mirror (DMLP505 Thorlabs®). The lasers illuminate a digital micromirror device (DMD; V-7001, Vialux®). The DMD is divided into 1024×768 micromirrors with a pitch of 13.7 µm. The angle of incidence of the beam is fine-tuned to maximise the output power. To maximise the illumination of the active surface of the DMD, the two beams are extended four times using a two-lens telescope (LA1131-A, f = 50 mm; LA1708-A, f = 200 mm; Thorlabs®). Finally, we compress the beam reflected by the DMD twice, using another telescope composed of a lens (LA1131-A f = 50 mm; Thorlabs®) and an objective (Olympus RMS4X, 0.1 NA). To cope with diffraction, we placed a diaphragm

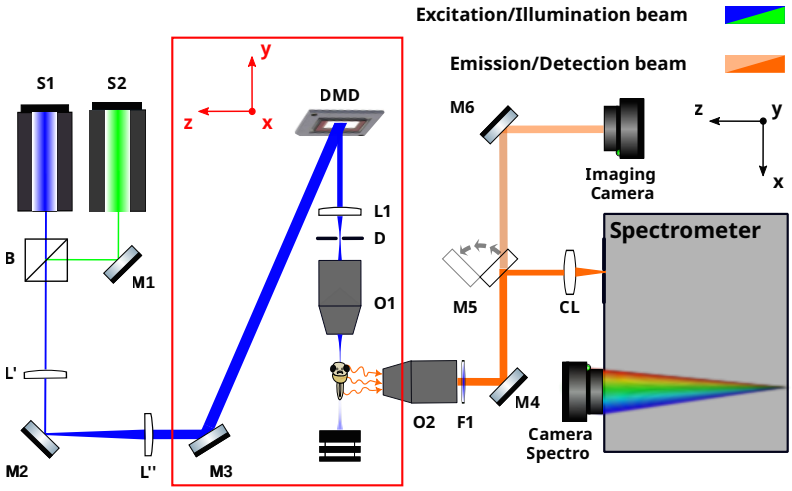

Fig. 1: Optical layout of the hyperspectral structured LSFM demonstrator. The beam from the lasers S1 and S2 illuminates a digital micromirror device (DMD). The reflected light is then focused into the sample. The fluorescence from the plane illuminated by the light sheet is collected by an objective and then either (spectral arm) focused on the spectrometer slit by a cylindrical lens (CL) or (grayscale arm) directly measured by the imaging camera. Note that the optical components in the red frame are perpendicular to the other components of the optical setup. B: Beam splitter; D: Diaphragm; F: Filter; L: Lens; M: Mirror; O: Objective, S: Sample.

between the lens and objective (see Section 2 below for further details). The fluorescence is collected through an objective lens (Olympus RMS4X, 0.1 NA). To eliminate any stray laser light and collect only the fluorescence from the sample, two notch filters (ZET473NF and ZET532NF, Chroma®) are placed after the collection objective. The fluorescence is then directed either to direct imaging (grayscale arm) or to an imaging spectrometer (spectral arm). The spectral arm includes a cylindrical achromatic lens (ACY254-075-A; Thorlabs®) that focuses the imaging plane of the light sheet onto the slit of a Czerny-Turner type imaging spectrometer (Shamrock 500i Andor®), mounted with a 300 line/mm grating (SR5-GRT-0300-0422; Andor®), followed by another camera (Andor Zyla-5.5). The spectrometer input slit is adjusted to maximise the incoming signal, giving a spectral resolution of 2 nm. Both arms of the setup are calibrated to observe the same field of view.

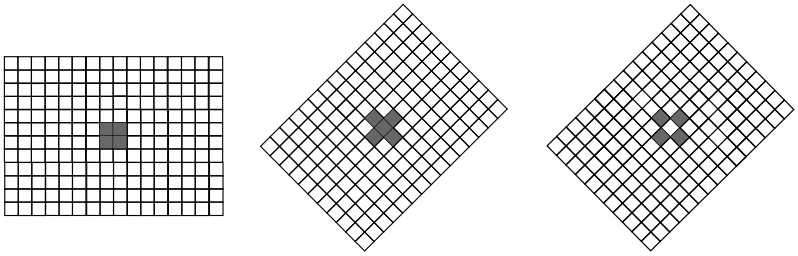

(a) Target pattern (b) Full tiling (c) Sparse tiling

Fig. 2: Pattern mapping on a grid rotated by 45°. (a) Square pattern on a classic rectangular grid. (b) Square pattern mapped onto a rotated grid with full tiling. (c) Square pattern mapped onto a rotated grid with sparse tiling.

2 Handling DMD diffraction

The light reflected by the DMD is subject to diffraction, in particular with coherent light sources. Therefore, the incident energy is spread across several diffraction orders corresponding to different reflection angles defined from the normal of the DMD (see Fig. 3c–d).

As the DMD micromirrors rotate around their diagonal, the DMD has to be tilted by 45° to keep the incident and reflected light in the same plane. Therefore, all the diffraction orders are shifted compared to the optical axis. To generate the pattern loaded onto the DMD we have to map a pattern initially created on a classic rectangular grid (Fig. 2a) onto a 45° rotated rectangular grid. Full tiling, using all DMD pixels (see Fig. 2b) and sparse tiling, using half of the DMD pixels (see Fig. 2c) were studied.

In order to study the influence of tiling on the orders of diffraction, we uploaded a uniform rectangular pattern onto the DMD, which corresponds to the first Walsh-Hadamard pattern (see Fig. 3a–b) and placed a screen after the DMD (see Fig. 3c–d). We observe that full tiling results in only the odd orders of diffraction (see Fig. 3c) while sparse tiling results in all orders of diffraction (see Fig. 3d). We retain the sparse tilling method as it allows access to even diffraction orders, in particular the zero-th order, whose interest in discussed in the next paragraph.

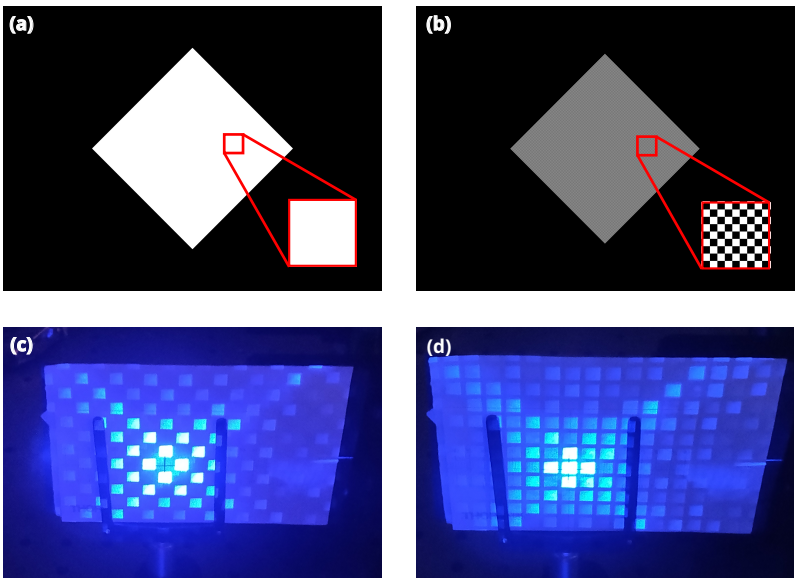

Fig. 3: Influence of rotation of the DMD patterns. (a-b) Patterns uploaded onto the DMD to generate the first Walsh-Hadamard pattern (all-ones pattern). The Walsh-Hadamard pattern is rotated by 45°. (a) Rotation with full tiling. (b) Rotation with sparse tiling. (c) Diffraction orders observed with the full tiling used in (a). (d) Diffraction orders observed with the sparse tiling used in (b).

To ensure the illumination profile remains constant along the optical axis, we filter the light reflected by the DMD with a diaphragm. The influence of the size of the aperture is illustrated in Figure 4. By selecting only the zero-th diffraction order, the light sheet is dimmer but more uniform around the focal plane of the illumination objective. By selecting more diffraction orders, the light sheet is brighter and sharper around the focal plane of the illumination objective, but its profiles vary more rapidly along the optical axis. In the following, we retain only the zero-th diffraction order to maximise illumination uniformity along the optical axis.

3 Light sheet characterisation

The thickness of the light sheet can be controlled by choosing the size of the pattern uploaded onto the DMD, as shown in Figure 5a–b. Our hyperspectral structured LSFM

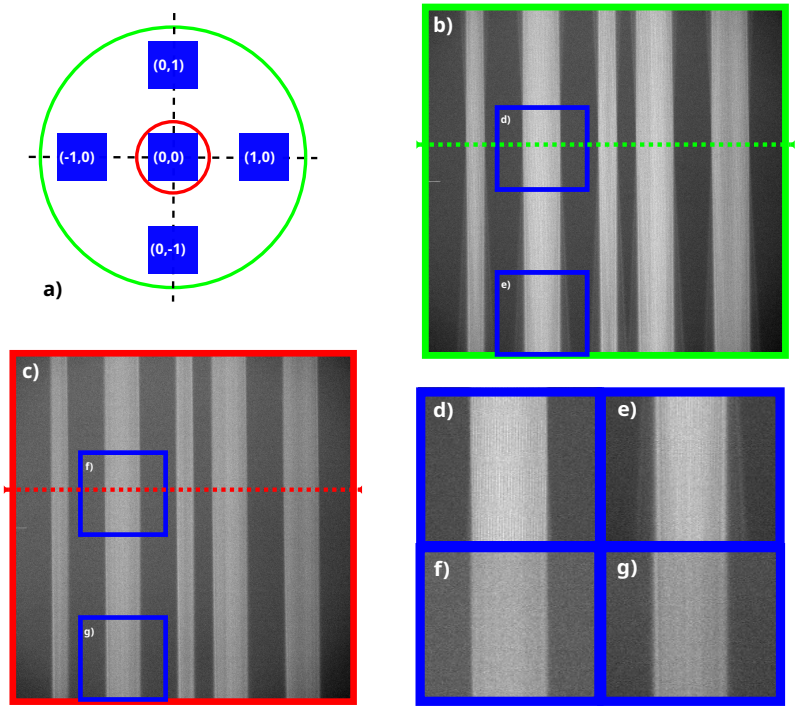

Fig. 4: Influence of the size of the aperture. (a) A diaphragm is used to filter out diffraction orders from the DMD; we schematise in green a wide aperture that retains the first five diffraction orders and in red a small aperture that retains only the zero-th order. (b) Illumination patterns obtained when considering a large diaphragm that selects the five orders denoted (0, 0), (1, 0), (0, 1), (-1, 0) and (0, -1) in (a). (c) Illumination patterns obtained considering a small diaphragm that selects only the order denoted (0, 0) in (a). The green and red dotted lines in (b) and (c) represent the plane where the DMD orders are refocused. (d, e) Zoom of two regions of the illumination patterns in (b). (f, g) Zoom of the same two regions of the illumination patterns in (c). By selecting only the zero-th diffraction order, the light sheet is dimmer but more uniform around the focal point of the objective. By selecting more diffraction orders, the light sheet is brighter, but its profiles vary more rapidly along the optical axis.

set-up allows the thickness and transverse illumination patterns of the light sheet to be characterised by measuring a homogeneous fluorescent solution using the grayscale arm. In the following, we consider a rhodamine solution. By rotating the patterns uploaded onto the DMD by 90°, the light sheet is also rotated and its cross section can be imaged with the imaging arm, as shown in Figure 5c–e. As shown in Table 1, we report the thickness of the light sheet as a function of the height of the patterns that are uploaded onto the

Table 1: Light sheet thickness for different heights of DMD patterns.

Height of DMD patterns (in pixels)	16	8	4	2	1
Light sheet thickness (in µm)	108	55	26	12	8

DMD. By decreasing the height of the DMD patterns from 16 to 1 micromirrors, the thickness of the light sheet, measured as the full width at half maximum (FWHM) at the focal spot, is decreased from 108 to 8 µm.

Both the target patterns and experimentally acquired patterns are shown in Figure 6. For the target patterns, we consider the $K = 128$ Walsh-Hadamard patterns displayed in Figure 6a. We recall that the Walsh-Hadamard patterns $\boldsymbol{H}$ contain negative values that cannot be implemented using a DMD. Therefore, we split $\boldsymbol{H}$ into two positive matrices $\boldsymbol{H}_+ = \max(\boldsymbol{H}, \boldsymbol{0})$ and $\boldsymbol{H}_- = \max(-\boldsymbol{H}, \boldsymbol{0})$ such that $\boldsymbol{H} = \boldsymbol{H}_+ - \boldsymbol{H}_-$ (see Section 9 for further details). The positive and negative patterns $\boldsymbol{H}_+$ and $\boldsymbol{H}_-$ were rotated using sparse tilling, repeated across a height of 16 pixels, uploaded onto the DMD, and measured in coumarin solution. Then, each pattern was integrated along the y-axis and resampled along the x-axis to get $N_x = 512$ pixels, leading to the experimentally acquired matrix shown in Figure 6b. We found that the experimental matrix is similar but not identical to the target matrix. For instance, the condition number of the matrix $\boldsymbol{H}$ is 1 for the target patterns and 4.3 for the experimental patterns.

4 Resolution of the imaging system

To characterise the spatial resolution of our device, we imaged an agarose solution containing fluorescent microspheres. The solution contains red and yellow-green fluorescent microspheres with a diameter of approximately 300 nm (Duke Scientific Polymer R300 Microspheres 0.3 µm and Polysciences Inc. Fluoresbrite® YG Microspheres 0.3 µm, both from Thermofisher®). The image obtained with the grayscale arm of our device is shown in Figure 7a, while that obtained with the hyperspectral imaging arm is shown Figure 7b. We reconstruct the hypersectral image by inversion of Eq. 1 of the main document in the

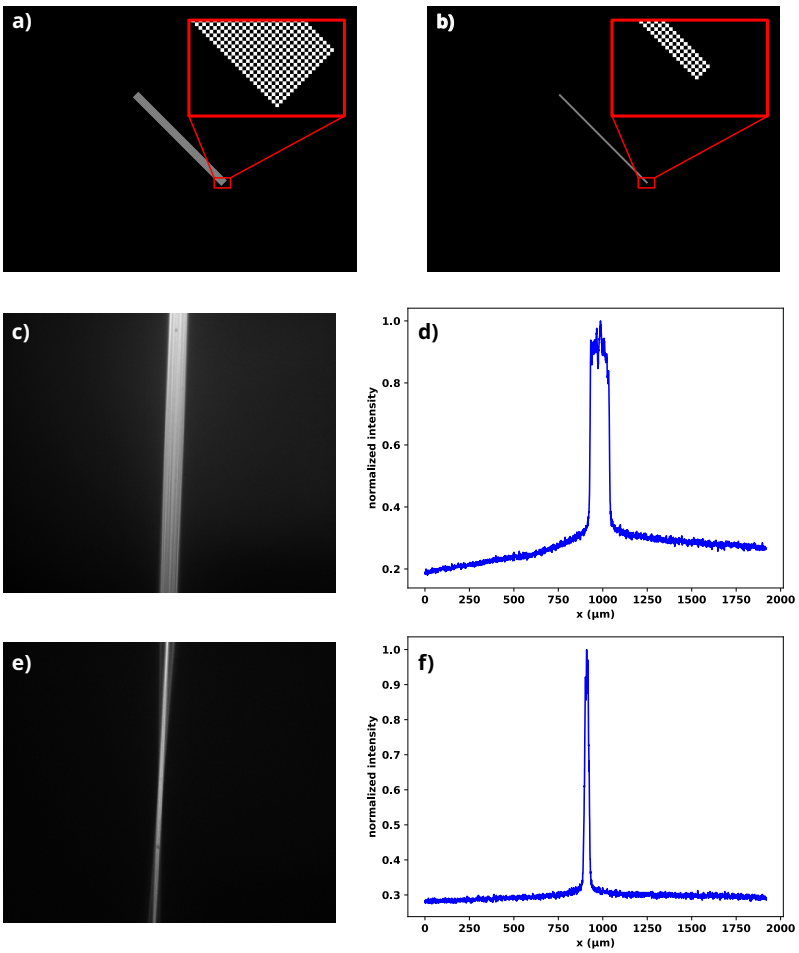

Fig. 5: Thickness of the light sheet. (a-b) DMD patterns with heights of 16 pixels (a) and 4 pixels (b). (c-d) Light sheets obtained for a 16-micromirror high DMD pattern; (c) Image of the light sheet; (d) Profile at central height where we measure a thickness of 108 µm (FWHM). (e-f) Light sheet obtained for a 4-micromirror high DMD pattern; (e) Image of the light sheet; (f) Profile at central height where we measure a thickness of 26 µm (FWHM). The DMD patterns are generated using sparse tiling.

least squares sense (pseudoinverse). For comparison purposes, we integrate the hyperspectral image over the spectral dimension. We selected two beads with the smallest spatial extent among all beads and clusters of beads observed in the field of view. In Figure 7c–d, we plot the profiles across the centres of the beads. We estimate the resolution along the x- and y-axis by measuring the FWHM of the profiles in the corresponding direction,

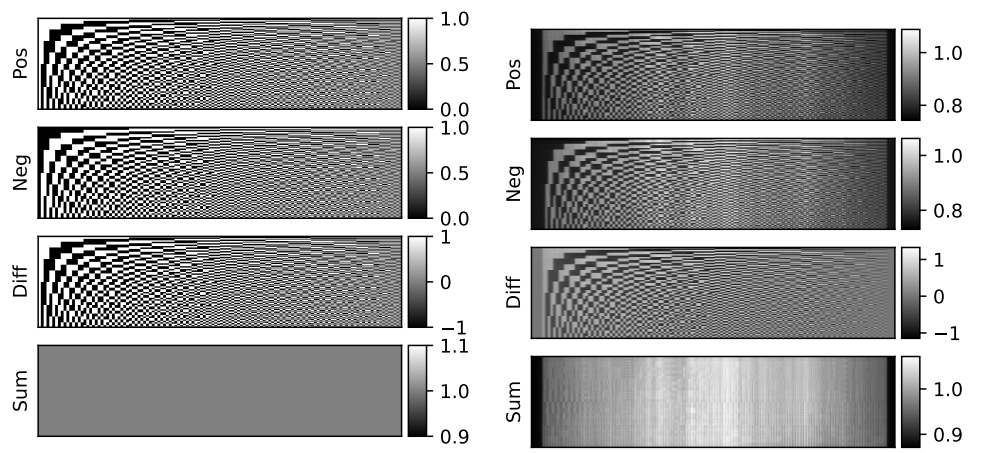

(a) Target patterns (b) Experimental patterns

Fig. 6: Graphical representation of the acquisition matrix. (a) Target Walsh-Hadamard matrix used to generate the DMD patterns. (b) Experimentally acquired matrix measured in rhodamine solution using the graycale arm. From top to bottom, we represent the positive component of the patterns $\boldsymbol{H}_+$ ('Pos'), the negative component of the patterns $\boldsymbol{H}_-$ ('Neg'), the difference $\boldsymbol{H} = \boldsymbol{H}_+ - \boldsymbol{H}_-$ ('Diff'), and the sum $\boldsymbol{H}_+ + \boldsymbol{H}_-$ ('Sum'). Both the sum and difference of the experimental patterns are normalised such that their first row has a mean value of 1. The acquisition matrix considered for spatial reconstruction (see Eq. 1 of the main document) is the difference of the experimental patterns.

which characterises the impulse response of the system, also know as point spread function (PSF). In the case of the conventional LSFM images acquired with the grayscale arm, the PSF can be modelled as a 2D isotropic Gaussian function. We measure the following resolutions : $\sigma_x^{\mathrm{A}} = 4$ µm, $\sigma_y^{\mathrm{A}} = 4$ µm, $\sigma_x^{\mathrm{B}} = 4$ µm and $\sigma_y^{\mathrm{B}} = 4$ µm, for the beads "A" and "B", respectively. In comparison, the PSF of the hyperspectral arm is more elongated along the y-axis than the x-axis (see Fig. 7b). Along the y-axis, we observe a Gaussian-like impulse response, while the impulse response along the x-axis exhibits side lobes (see Fig. 7d). We measure the following resolutions : $\sigma_x^{\mathrm{A}} = 15$ µm, $\sigma_y^{\mathrm{A}} = 6$ µm, $\sigma_x^{\mathrm{B}} = 15$ µm and $\sigma_y^{\mathrm{B}} = 7$ µm.

Comparing the spatial resolution of the hyperspectral and grayscale arm, we observe a similar resolution along the y-axis, while the spatial resolution of the hyperspectral arm is 3 times greater than that of the grayscale arm along the x-axis. The spatial resolution

Table 2: Spatial resolution of hyperspectral structured LSFM as a function of number of patterns. Profiles analysed across the "A" bead.

Number of patterns K	32	64	128
x-axis resolution σ_x^{A} (µm)	77	36	15
y-axis resolution σ_y^{A} (µm)	6	6	6

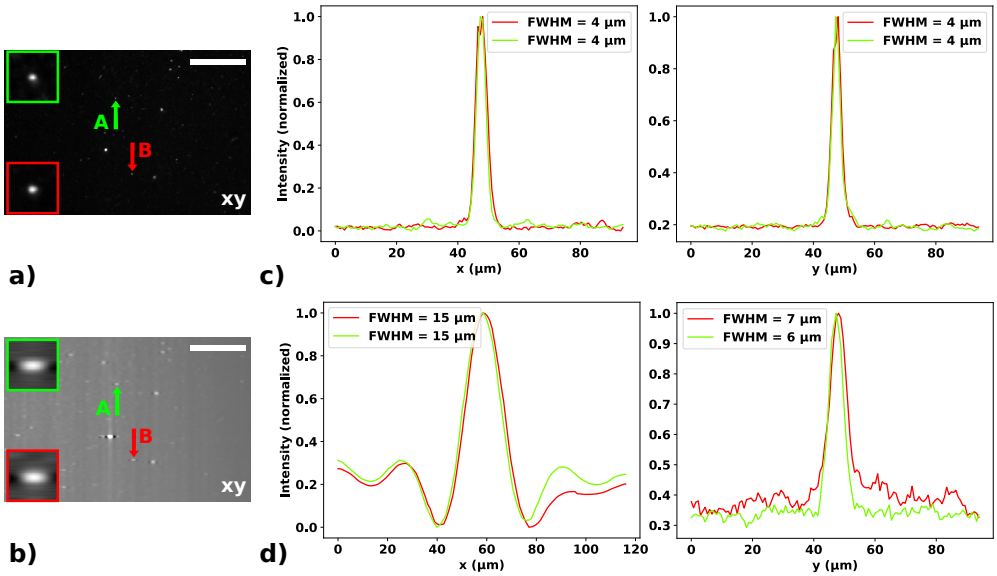

Fig. 7: Spatial resolution of the grayscale and hyperspectral arms. We image an agarose solution containing fluorescent microspheres using (a) the grayscale arm and (b) the hyperspectral arm using 128 patterns. We integrate the hyperspectral image over the spectral dimension. Scale bars represent 100 µm. We select two beads (labelled 'A' and 'B' and indicated with arrows in (a) and (b). The red and green boxes show the beads A and B magnified 4 times. We plot the intensity profiles across the centre of the beads in the x- and y-direction for (c) the grayscale arm and (d) the hyperspectral arm.

of the hyperspectral arm along the x-axis is related to the number of measured patterns. Therefore, we have evaluated the spatial resolution of the hyperspectral arm for different numbers of patterns (see Table 2). As expected, we observe that the x-axis resolution depends linearly on the number of patterns, while the y-axis resolutions remains constant.

To evaluate the spectral resolution, the two lasers (473 nm and 532 nm) were directed onto the entrance slit of the spectrometer; the spectral resolution was measured to be 2 nm FWHM.

5 Acquisition speed

In Table 3, we report the relevant acquisition parameters to evaluate the acquisition speed for all samples considered in this study. The parameters are interrelated: the exposure time depends on the laser power (higher power leads to shorter time and vice versa), as well as on the number of (spatial) pixels and spectral channels in the acquisition. Therefore, we introduce the power-time budget per pixel b as a speed metric:

$$b = \frac{PT}{\Lambda N}, \tag{1}$$

where P is the light power, T the acquisition time, Λ the number of spectral channels and N the number of pixels. For Tg(fli1:EGFP;olig2:DsRed) (i.e., Zebraf1 in Table 3) the power-time budget per pixel of hyperspectral structured LSFM is $2560 \cdot 10^3 \cdot (55+95)/(128 \cdot 512 \cdot 128) = 46$ µW.ms/pixel; for Tg(sox10:mRFP;olig2:DsRed) (i.e., Zebraf2 in Table 3) the power-time budget per pixel of hyperspectral structured LSFM is $512 \cdot 10^3 \cdot 640/(128 \cdot 512 \cdot 128) = 39$ µW.ms/pixel. Considering that 2048 spectral channels are acquired in the raw data (128 channels after binning), hyperspectral structured LSFM achieves even lower power-time budgets per pixel. Substituting $\Lambda = 2048$ instead of $\Lambda = 128$ in the above calculations, we get budgets of 2.9 µW.ms/pixel and 2.5 µW.ms/pixel, respectively. We can compare the power-time budget per pixel of hyperspectral structured LSFM to that of the method in [1]. Assuming four lasers with 5 mW power each were used in [1], that method achieves a power-time budget per pixel of $4 \cdot 5 \cdot 10^3 \cdot 1.5 \cdot 10^3/(2000 \cdot 70) = 214$ µW.ms/pixel, which is one or two orders of magnitude slower than hyperspectral structured LSFM.

Table 3: Acquisition parameters for all samples considered in this study. Laser 1 emits at 532 nm, laser 2 at 473 nm. Zebraf1 corresponds to Tg(fli1:EGFP;olig2:DsRed), Zebraf2 to Tg(sox10:mRFP;olig2:DsRed).

Sample	Acquisition system	Exposure (in s/slice)	Laser 1 (in µW)	Laser 2 (in µW)
Beads	LSFM	4	42	87
Beads	hyperspectral structured LSFM	512	42	87
Zebraf1	LSFM	2	55	95
Zebraf1	hyperspectral structured LSFM	2560	55	95
Zebraf2	LSFM	1	0	640
Zebraf2	hyperspectral structured LSFM	512	0	640

6 Three-dimensional acquisitions

The 3D representation of the zebrafish embryos in Fig. 2c and Fig. 3c of the main document are obtained from 20 and 25 slices, respectively. In Fig. 8, we display the abundance maps of EGFP and DsRed for several slices of the Tg(fli1:EGFP;olig2:DsRed) embryo, while we display the corresponding conventional LSFM images in Fig. 9. In Fig. 10, we display the abundance maps of mRFP and DsRed for all slices of the Tg(sox10:mRFP;olig2:DsRed) embryo, while we display the corresponding conventional LSFM images in Fig. 11. We acquired all the slices by translating the samples with a 15 µm step. The depth of field of the collection objective was 55 µm and the height of the DMD pattern was 4 pixels, which corresponds to a thickness of 26 µm of the light sheet (see Table 1).

7 Verification of Fellgett's advantage

The first hyperspectral light sheet microscope involved scanning an illumination line within the imaging plane [1], known as push-broom scanning in hyperspectral literature. Here, we propose the illumination of multiple lines at the same time to benefit from the signal-to-noise ratio improvement provided by multiplexed acquisitions [2]. To verify this improvement experimentally, we compare the images obtained from Hadamard patterns to those obtained from push-broom patterns (see Fig. 12). We consider $K = 64$ push-broom patterns and $K = 64$ Hadamard patterns with positive and negative components

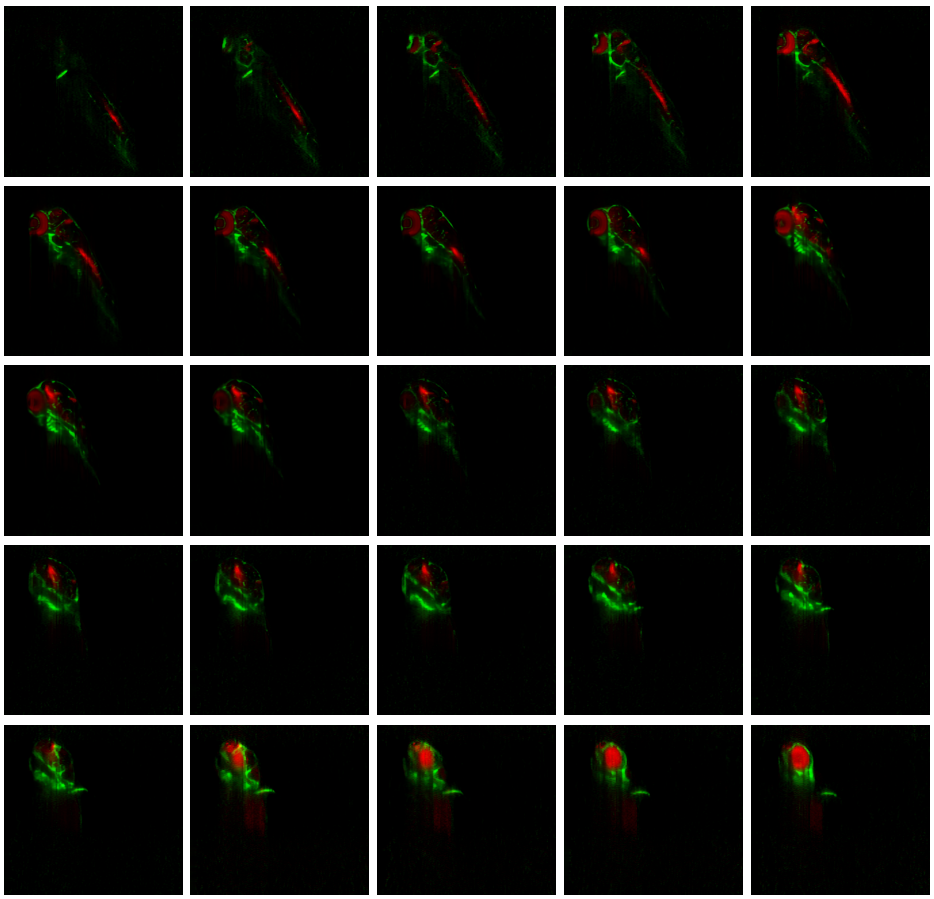

Fig. 8: Quantitative abundance maps of DsRed (in red) and EGFP (in green) obtained by translating the Tg(fli1:EGFP;olig2:DsRed) zebrafish larva with a translation step of 15 µm. The slices were used to generate the 3D representation in Figure 2c of the main document.

measured independently. The integration time is set to 8 s for push-broom patterns and 4 s for Hadamard patterns, resulting in a total acquisition time of 512 s for both cases.

The hyperspectral images reconstructed at six detection wavelengths ranging from 510 to 594 nm are shown in Figure 12. We confirm that Hadamard patterns provide improved image quality across all wavelengths investigated. Felgett's advantage appears more evident at low counts compared to high counts (compare Fig. 12a to b at 510 nm, where the lowest signal is obtained, and at 534 nm where the highest signal is measured). To quantify Felgett's advantage, the peak signal-to-noise ratio is computed at each wavelength by

Fig. 9: Conventional LSFM images corresponding to the last slices in Fig. 8. The sample is the Tg(fli1:EGFP;olig2:DsRed) zebrafish larva. The translation step is 15 µm.

dividing the maximum intensity by the standard deviation in a background region where no fluorescence is observed. We obtain an improvement of 8.9, 8.9, 8.1, 7.7, 8.5, 7.7, 8.3, and 8 dB at 510, 522, 534, 558, 582, and 594 nm, respectively.

8 Raw measurement noise model

Following a common approach in single-pixel imaging, we split the measurement matrix[1] into two positive matrices $\boldsymbol{H}_+ = \max(\boldsymbol{H}, \boldsymbol{0})$ and $\boldsymbol{H}_- = \max(-\boldsymbol{H}, \boldsymbol{0})$ such that $\boldsymbol{H} = \boldsymbol{H}_+ - \boldsymbol{H}_-$. We then acquire the "positive" measurements $\boldsymbol{m}_+$ and the "negative" measurements $\boldsymbol{m}_-$ by uploading, respectively, $\boldsymbol{H}_+$ and $\boldsymbol{H}_-$ on the DMD. The

[1]The Hadamard matrices contain negative values that cannot be implemented using a DMD

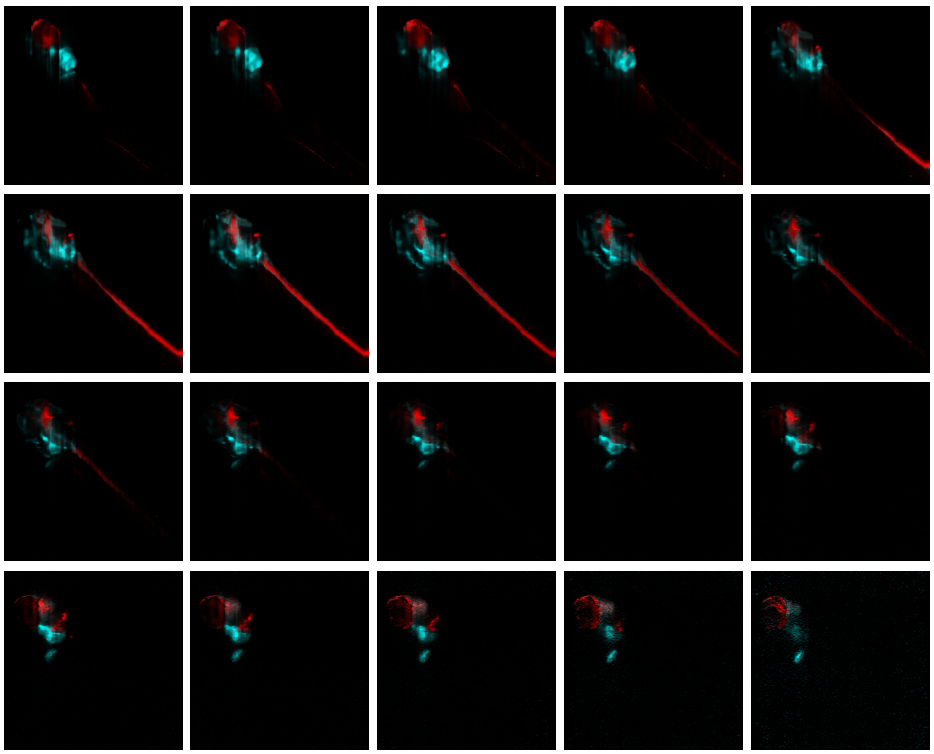

Fig. 10: Quantitative abundance maps of DsRed (in red) and mRFP (in cyan) obtained by translating the Tg(sox10:mRFP;olig2:DsRed) zebrafish larva with a translation step of 15 µm. The slices were used to generate the 3D representation in Figure 3c of the main document.

measurements are corrupted by mixed Poisson-Gaussian noise [3]

$$\mathbf{m}_+ \sim g\,\mathcal{P}(\alpha \boldsymbol{H}_+ \boldsymbol{f}) + \mathcal{N}(\mu_\mathsf{d}, \sigma_\mathsf{d}^2), \tag{2a}$$

$$\mathbf{m}_- \sim g\,\mathcal{P}(\alpha \boldsymbol{H}_- \boldsymbol{f}) + \mathcal{N}(\mu_\mathsf{d}, \sigma_\mathsf{d}^2), \tag{2b}$$

where $\mathcal{P}$ and $\mathcal{N}$ are the Poisson and Gaussian distributions, g is a constant that represents the overall system gain (in counts/electron), α is the image intensity (in photons), $\boldsymbol{f} \in [0,1]^{N_x}$ the (unknown) image row, μ_d is the dark current (in counts), and σ_d is the dark noise (in counts). The scalars g, μ_d and σ_d can be estimated prior to measurement.

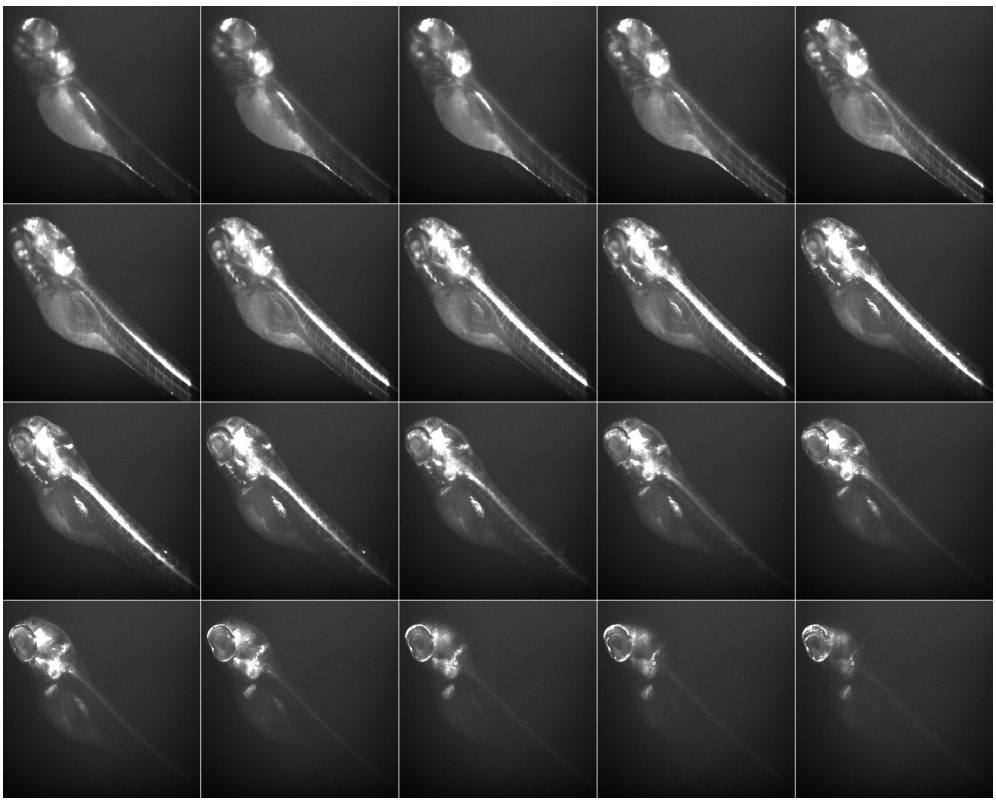

Fig. 11: Conventional LSFM images corresponding to the slices in Fig. 10. The sample is the Tg(sox10:mRFP;olig2:DsRed) zebrafish larva. The translation step is 15 µm.

9 Preprocessed measurements

The measurements introduced in Eq. 1 of the main document are differential measurements computed from the raw measurements as

$$\boldsymbol{m} = \frac{\boldsymbol{m}_+ - \boldsymbol{m}_-}{\alpha g}. \tag{3}$$

Interestingly, we have $\mathbb{E}(\boldsymbol{m}) = \boldsymbol{H}\boldsymbol{f}$. The use of differential measurements therefore allows the DC component of the measurements to be rejected, while normalisation ensures that the nonlinear mapping (e.g., neural network) of Eq. 5 of the main document is insensitive to image intensity. Insensitivity to image intensity is particularly useful when different

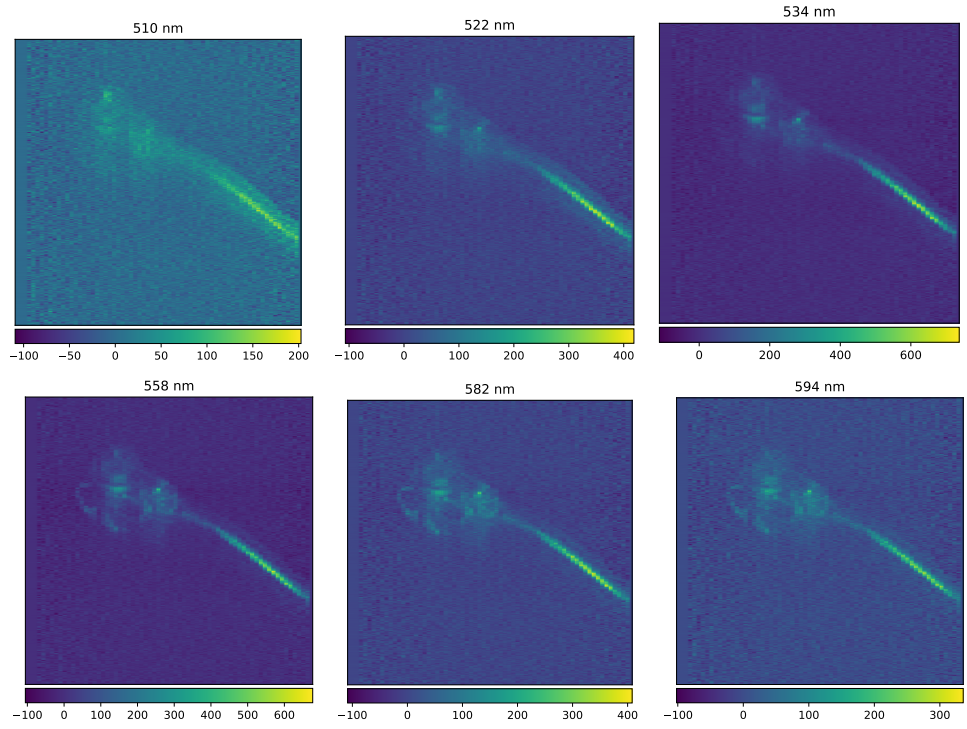

(a) Hyperspectral images obtained from push-broom patterns

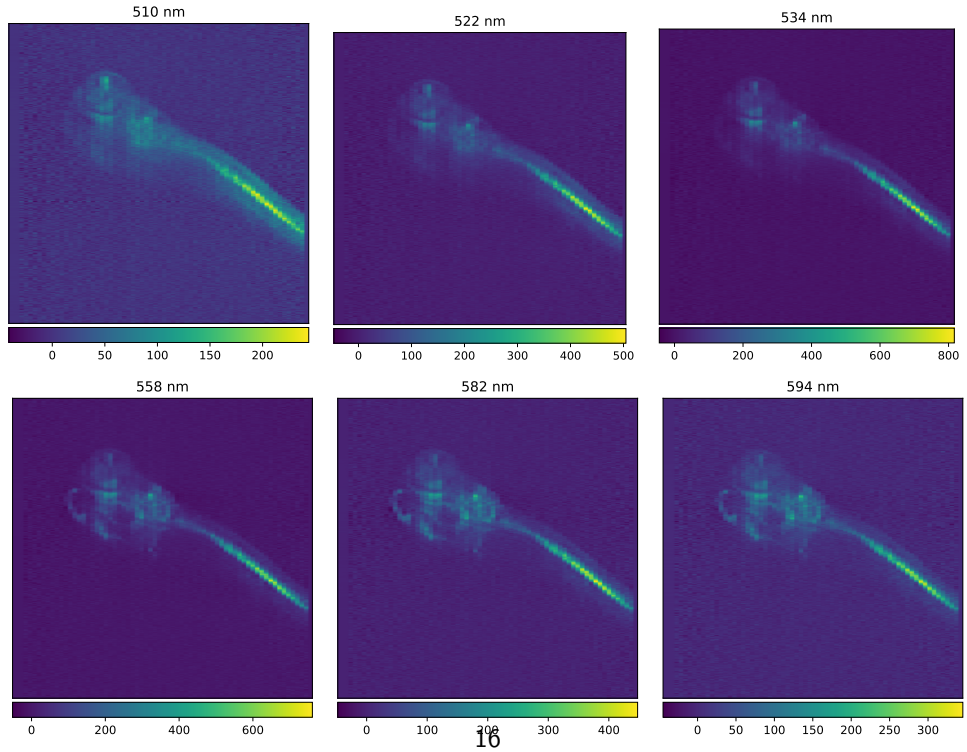

(b) Hyperspectral images obtained from Hadamard patterns

Fig. 12: Comparison between push-broom and Hadamard patterns. We consider $N = 64$ push-broom patterns and $N = 64$ Hadamard patterns with positive and negative components measured independently. The integration time is set to 8 s for push-broom patterns and 4 s for Hadamard patterns, resulting in a total acquisition time of 512 s for both cases. Hyperspectral image reconstructed at six central wavelengths: 510, 522, 534, 558, 582, and 594 nm. The colour bars indicate the photon counts, which vary across images. All images are reconstructed by inversion of Eq. 1 of the main document in the least squares sense (pseudoinverse). The sample is the 4-day-old Tg(sox10:mRFP;olig2:DsRed) zebrafish larva considered in Section 2.5 of the main document.

spectral images acquired at different wavelengths are reconstructed with the same neural network. While g can be calibrated, the image intensity has to be estimated from the raw measurements, as described below.

To estimate the image intensity, we note that the expectation of the sum of raw measurements is given by $\mathbb{E}(\mathbf{m}_+ + \mathbf{m}_-) = \alpha g(\boldsymbol{H}_+ + \boldsymbol{H}_-)\boldsymbol{f} + 2\mu_\mathsf{d}$. In the case of Hadamard patterns, we have $\boldsymbol{H}_+ + \boldsymbol{H}_- = \boldsymbol{J}$, where $\boldsymbol{J}$ is the all-ones matrix. Therefore, all of the K components of $\mathbf{m}_+ + \mathbf{m}_-$ have the same expected value $\alpha g f_\mathsf{tot} + 2\mu_\mathsf{d}$, where $f_\mathsf{tot} = \sum_n^{N_x} f_n$ is the total intensity. This suggests that the intensity can be computed as $\alpha = \frac{1}{g f_\mathsf{tot}}((\frac{1}{K}\sum_{k=1}^{K} \boldsymbol{m}_{+,k} + \boldsymbol{m}_{-,k}) - 2\mu_\mathsf{d})$. We then further note that f_tot cannot be larger than N_x, which provides a lower bound for α. In the case of experimental patterns (see Fig. 6), the sum-to-one property is no longer satisfied; however, we find that $\boldsymbol{H}_+ + \boldsymbol{H}_- \approx \frac{1}{2}\boldsymbol{J}$ is a good approximation. We therefore approximate $f_\mathsf{tot} \approx \frac{N_x}{2}$, leading to

$$\alpha = \frac{2}{gN_x}\left(\left(\frac{1}{K}\sum_{k=1}^{K} \boldsymbol{m}_{+,k} + \boldsymbol{m}_{-,k}\right) - 2\mu_\mathsf{d}\right). \tag{4}$$

10 Estimation of the covariance matrices

Image covariance

We estimate the covariance matrix $\boldsymbol{\Sigma} \in \mathbb{R}^{N_x \times N_x}$ used in Eq. 4 of the main document by computing the sample covariance. We consider each column in each image of the ImageNet validation set as an independent sample and compute the sample covariance as

$$\boldsymbol{\Sigma} = \frac{1}{LN_y - 1}\sum_{\ell=1}^{L}\sum_{j=1}^{N_y}(\boldsymbol{f}_j^\ell - \boldsymbol{\mu})^\top(\boldsymbol{f}_j^\ell - \boldsymbol{\mu}), \tag{5}$$

where $\boldsymbol{f}_j^\ell \in \mathbb{R}^{N_x}$ represents the j-th column of the image $\boldsymbol{F}^\ell \in \mathbb{R}^{N_x \times N_y}$ and $\boldsymbol{\mu} = \frac{1}{LN_y}\sum_\ell \sum_j \boldsymbol{f}_j^\ell$ is the mean column. All images are normalised in $[0,1]^{N_x}$.

Measurement covariance

Assuming independent measurements, the measurement covariance $\boldsymbol{\Gamma} = \mathbb{C}\mathrm{ov}\,(\boldsymbol{m})$ is given by $\frac{1}{(\alpha g)^2}\left[\mathbb{C}\mathrm{ov}\,(\mathbf{m}_+) + \mathbb{C}\mathrm{ov}\,(\mathbf{m}_-)\right] = \frac{1}{\alpha}\mathrm{Diag}\left((\boldsymbol{H}_+ + \boldsymbol{H}_-)\boldsymbol{f}\right) + \frac{2}{(\alpha g)^2}\sigma_{\mathsf{d}}^2$. It can be noted that $\mathbb{C}\mathrm{ov}\,(\mathbf{m})$ depends on the unknown image $\boldsymbol{f}$. A standard approach to circumvent this problem is to approach the signal-dependent variance by a signal-independent variance estimated from the measurements. We recall that the expectation of the sum of raw measurements is given by $g(\boldsymbol{H}_+ + \boldsymbol{H}_-)\boldsymbol{f} + 2\mu_{\mathsf{d}}$. As suggested in [4], we substitute the expected values by the noisy samples[2], leading to

$$\boldsymbol{\Gamma} \approx \frac{1}{g\alpha^2}\left[\mathrm{Diag}\,(\boldsymbol{m}_+ + \boldsymbol{m}_-) - 2\mu_{\mathsf{d}}\right] + \frac{2}{(\alpha g)^2}\sigma_{\mathsf{d}}^2. \tag{6}$$

This approximation is acceptable for high photon counts, i.e., when the components of $(\boldsymbol{H}_+ + \boldsymbol{H}_-)\boldsymbol{f}$ are large, which is the case, in practice, where typical photon counts are between 1,000 and 10,000.

References

[1] Jahr, W., Schmid, B., Schmied, C., Fahrbach, F.O., Huisken, J.: Hyperspectral light sheet microscopy. Nature Communications **6**, 7990 (2015) https://doi.org/10.1038/ncomms8990

[2] Sloane, N.J.A., Harwit, M.: Masks for Hadamard transform optics, and weighing designs. Applied Optics **15**(1), 107–114 (1976) https://doi.org/10.1364/AO.15.000107

[3] Association, E.M.V.: EMVA standard 1288, standard for characterization of image sensors and cameras. Release **3**, 29 (2016)

[2] Assuming $m \sim \mathcal{P}(\eta)$ where η is the expectation, it can be shown that $(m-\eta)/\sqrt{m} \to \mathcal{N}(0,1)$, as η tends to infinity (see Eq. 74 of [5]).

[4] Lorente Mur, A., Peyrin, F., Ducros, N.: Deep Expectation-Maximization for Single-Pixel Image Reconstruction With Signal-Dependent Noise. IEEE Transactions on Computational Imaging **8**, 759–769 (2022) https://doi.org/10.1109/TCI.2022.3200841

[5] Hohage, T., Werner, F.: Inverse problems with Poisson data: Statistical regularization theory, applications and algorithms. Inverse Problems **32**(9), 093001 (2016) https://doi.org/10.1088/0266-5611/32/9/093001